Variations of electric field and electric resistivity of air caused by dust motion

E. Seran,[1] M. Godefroy,[1] N. Renno,[2] and H. Elliott[2]

Received 24 April 2013; revised 25 July 2013; accepted 26 July 2013; published 22 August 2013.

[1] We report results of a field campaign conducted in the Nevada desert with a suite of electric field instruments consisting of a field mill (FM) and a short dipole antenna (SDA). Furthermore, we show that a combination of the measurements of these two instruments allows the estimation of the electric resistivity of air, an important quantity that is extremely difficult to measure near the Earth's surface. The electric resistivity of air is found to vary between $1.5 \cdot 10^{13}$ and $6 \cdot 10^{13}$ Ω m and to correlate with changes in electric field. Vertical DC electric fields with amplitudes up to 6 kV m^{-1} were observed to correspond to clouds of dust blowing through the measurement site. Enhanced DC and AC electric fields are measured during periods when horizontal wind speed exceeds 7 m s^{-1}, or around twice the background value. We suggest that low-frequency emissions, below ~200 Hz, are generated by the motion of electrically charged particles in the vicinity of the SDA electrode and propose a simple model to reproduce the observed spectra. According to this model, the spectral response is controlled by three parameters, (i) the speed of the charged particles, (ii) the charge concentration, and (iii) the minimum distance between the particle and the electrode. In order to explain the electric fields measured with the FM sensors at different heights, we developed a multilayer model that relates the electric field to the charge distribution. For example, a nonlinear variation of the electric field observed by the FM sensors below 50 cm is simulated by a near-surface layer of tens of centimeters that is filled with electrically charged particles that carry a predominantly negative charge in the vicinity of the soil. The charge concentration inside this layer is estimated to vary between 10^{12} and $5 \cdot 10^{13}$ electrons m^{-3}.

Citation: Seran, E., M. Godefroy, N. Renno, and H. Elliott (2013), Variations of electric field and electric resistivity of air caused by dust motion, *J. Geophys. Res. Space Physics*, *118*, 5358–5368, doi:10.1002/jgra.50478.

1. Introduction

[2] Earth's atmosphere is a unique natural laboratory that offers a large variety of electric conditions and also multiple mechanisms which control the electrical features. From the ground to the upper stratosphere, the electric resistivity of air varies from ~10^{14} to ~10^{10} Ω m, while the DC electric field decreases from ~ 100 V m^{-1} to ~10 mV m^{-1}. Locally and during short periods of time, the electric field might grow up to ~100 kV m^{-1}. Such fields are observed during thunderstorms in the troposphere [*Stolzenburg and Marshall*, 1998; *Merceret et al*., 2008] or during dust activation phenomena in deserts [*Schmidt et al*., 1998; *Farrell et al*., 2003]. In the first case, high electric fields are the result of electric charging of atmospheric water droplets or ice crystals. In the second, these fields are generated by the triboelectric charging of dust and/or sand particles.

[3] Analysis of the electrical properties in dusty environments raises a number of questions related to the electric charging of the surface and airborne particles. Among various mechanisms (e.g., photoemission from a UV-illuminated surface, interaction with electrons, light ions, energetic particles and cosmic rays, electric charging induced by an electric field, etc.), the triboelectric charging is likely most efficient in such an environment. Laboratory experiments with different types of nonconducting 100 μm grains (including lunar and Martian regolith simulants) [*Sickafoose et al*., 2001] demonstrated that because of the triboelectrical effect (i) the particles are efficiently charged and might carry up to 10^5 elementary charges, (ii) the number of negatively and positively charged particles is nearly equal, and (iii) the mineral composition of grains determines their electric features. Naturally, the triboelectric charging is efficient when individual particles move with respect to one another. This motion can be driven by winds, pressure and temperature gradients, and electric and/or gravitational forces. Depending on the forces and also on the grain size, the particles available at the surface might be involved in different types of motion such as rolling, blowing, saltating, and/or vertical, spiral or shearing motion [e.g., *Greeley and Iversen*, 1985; *Metzger*, 1999; *Metzger et al*., 2011; *Kok and Renno*, 2006, 2008; *Schmidt et al*., 1998; *Farrell et al*., 2004]. The size of the transported particles typically ranges from a few micrometers to a few millimeters.

[1]LATMOS/IPSL/UVSQ/UPMC, Paris, France.
[2]SPRL, University of Michigan, Ann Arbor, Michigan, USA.

Corresponding author: E. Seran, LATMOS/IPSL/UVSQ/UPMC, 4 place Jussieu, FR-75252 Paris CEDEX 05, France. (Elena.Seran@latmos.ipsl.fr)

2169-9380/13/10.1002/jgra.50478

Following the definition given by *Metzger* [1999], "dust" (or fines) is broadly defined as fine soil material less than ~100 μm in diameter and thus includes fine sand, silt, and clay. Soil material with larger diameters (up to ~2 mm) is usually referred to as "sand" (or sand-size grains). This material is often the result of the aggregation of smaller particles. Sand-sized particles are easily transported along the surface (staying in contact with the surface or bouncing) by winds due to their lower cohesive attraction to other surface material. Relatively larger protuberances into the wind stream generally amplify this transport. Having the ability to become lifted, sand is usually considered the main loading material for thermally raised air convection (e.g., thermal plumes, thermal vortices) caused by the heating of the near-surface air by insulation [*Metzger et al*., 2011; *Balme and Greeley*, 2006]. Dust, although a minority of the mass lifted by thermal vortices, readily remains airborne once eroded and can be transported for substantial distances (in contrast with sand which predominantly falls back to the surface relatively close to its entrainment origin). The resulting particle-loaded vertical convective vortices, called dust devils, are thus formed in the same way as thermal vortices, but are more effective at soil erosion than weaker thermal vortices. The total electric charge carried by the surface and the airborne particles might be very different depending on the transport mechanisms, strength of applied forces, dielectric proprieties of the soil material, and/or amount of available dust/sand on the surface. When the polarity of this electric charge becomes imbalanced, it results in the formation of an electric field. The electric fields measured in and/or near dust devils were used to estimate the charge density in the dust devil columns. According to estimations summarized by *Balme and Greeley* [2006], the charge density in the dust columns varies between $\sim 10^{11}$ and $\sim 10^{13}$ electrons m^{-3}. Dust devils always appear to have upward electric fields resulting from the separation of charges (negative on the top of dust column and/or positive on its bottom). Measurements of saltating sand with a Faraday cage drift trap at 5 cm above the surface [*Schmidt et al*., 1998] indicated a positive total charge of 60 μC kg^{-1} carried by the sand and an average mass flux of 8.5 10^{-3} kg $m^{-2}\,s^{-1}$. Taking into account the typical diameter of the collected sand (~150 μm) and the wind speed (~10 m s^{-1}), the average positive charge carried by an individual grain and the sand concentration are estimated to be approximately 10^6 electrons and $3 \cdot 10^5\ m^{-3}$, respectively.

[4] Understanding the electrical proprieties of dusty environments was the main motivation for this study. Two sets of electric field instruments were used. The first is a field mill (FM) designed to measure large DC electric fields (up to several hundred kV m^{-1}). The second is a short dipole antenna (SDA) designed to measure electric potential from DC to a few kHz, which is determined by the electric field and also by the electric resistivity of air. Thus, in principle, the combination of these two instruments gives the ability to measure not only the electric field but also the coupling resistance of the SDA electrode with the atmosphere, and thus the electric resistivity of air. Measuring the electric resistivity of air near the Earth's surface is not a simple task because of the very low mobility of light ions, the main carriers of electric charge in the lower atmosphere. For example, the relaxation method, routinely used to measure the electric resistivity of air in the stratosphere, does not work near the surface because the relaxation time (up to tens of minutes) is too long relative to the time scale of variations in the DC electric fields.

[5] The structure of this paper is as follows. We start with descriptions of each instrument (section 2), the field site, the soil properties, and the environmental conditions (section 3). In section 4, we present the FM measurements of the electric field at various heights and examine a number of mechanisms that might cause the observed height variations. In section 5, we compare the measurements of two electric field instruments, the FM and the SDA, deduce the coupling resistance of the SDA electrode with the atmosphere, and estimate the electric resistivity of air. Temporal variation in the frequency spectra of the electric potential measured by the SDA is compared with the DC electric field and wind speed in section 6. Then, a simple model is proposed to explain the observed increase of the electric potential in the ULF/ELF frequency range. The main findings are summarized in section 7.

2. Instrumentation

2.1. Field Mill (FM)

[6] The field mill used in our instrumental suite is a cylindrical rotational sensor [*Johnston and Kirkham*, 1989; *Renno et al*., 2008]. This type of sensor measures the amplitude and phase of the electric current at the frequency of the sensor's rotation (~20 Hz). These observations are then used to deduce the amplitude and the direction of the electric field at the sensor height and in the plane perpendicular to the sensor's axis. Four FM sensors are mounted on a 2 m tall vertical mast and provide simultaneous measurements of the electric field at 6, 55, 120, and 199 cm above the ground (Figure 1).

2.2. Short Dipole Antenna (SDA)

[7] The SDA used in our instrumental suite consists of three cylindrical electrodes mounted on the top of an electronic box with insulated masts 50 cm long (Figure 2a). The masts were designed so that they were sufficiently long (~2.8 times longer than the box height) to minimize electric perturbations induced by the electrically grounded body. The estimated perturbations do not exceed 1% (see Appendix A). The conducting box enclosing the electronics is electrically grounded and provides an electrical reference for the measurements made by each electrode. The ground around the SDA is covered with a conducting grid to ensure good electric contact between the electronic box and the ground and to force the potential at the ground to be uniform. Each electrode measures DC and AC (from 3 Hz to ~1 kHz) electric potentials with respect to the ground reference. Simultaneous measurements with the three electrodes are then used to calculate the three vector components of the electric field.

[8] The basic electronic design of the SDA instrument allows the measurement of the DC electric potential of each electrode varying from −100 V to +100 V. A simplified schematic of the SDA electrical configuration is shown in Figure 2b. The effective coupling of the SDA electrode to the atmosphere is represented by its resistance (R_2), the electrode by its capacitance (C_2), and the electronics board by its input capacitance (C_1) and its input resistance (R_1). In the configuration depicted in Figure 2b, the relationship between the

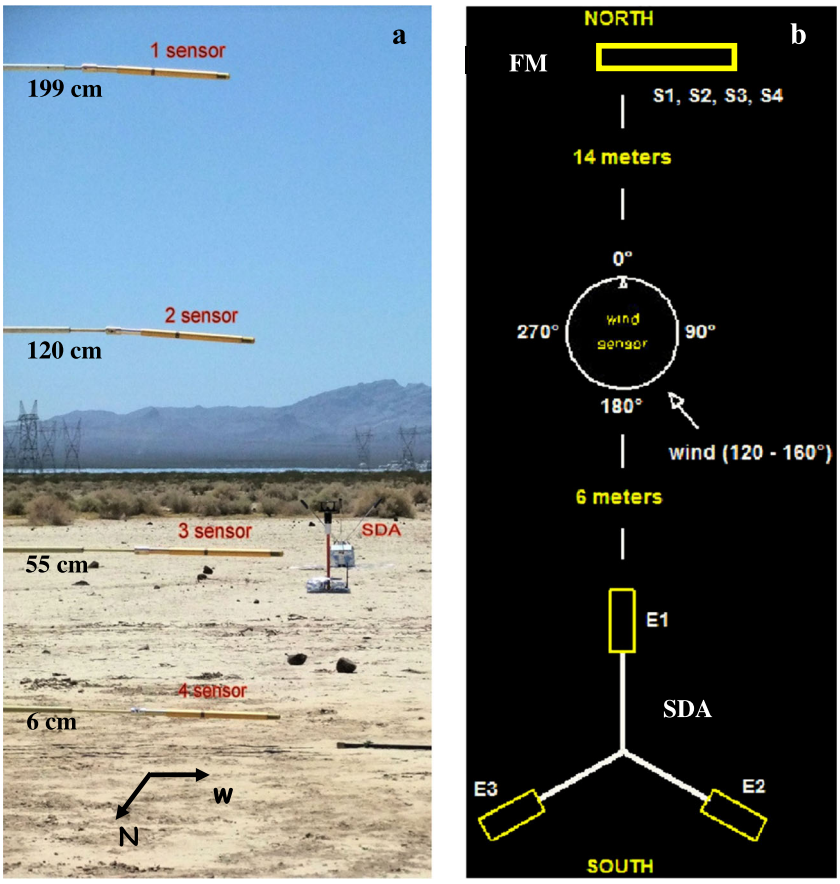

Figure 1. (a) FM sensors mounted on 2 m mast. (b) Accommodation of instruments.

potential being measured (φ_1) and the potential at the electrode height (φ_2) can be written as

$$\varphi_1/\varphi_2 = (1 + i\omega C_2 R_2)/((R_1 + R_2)/R_1 + i\omega(C_1 + C_2)R_2), \quad (1)$$

where ω is a circular frequency. Thus, at frequencies well below $[(C_1 + C_2)R_2]^{-1}$, $\varphi_1/\varphi_2 = R_1/(R_1 + R_2)$ and tends to 1 if the input resistance of the preamplifier R_1 (which is $>10^{15}$ Ω) is significantly higher than the coupling resistance R_2. At frequencies well above $[C_2R_2]^{-1}$, $\varphi_1/\varphi_2 = C_2/(C_1 + C_2)$. Using the capacitance values from the SDA, $C_1 = 2.2pF$ and $C_2 = 2.9pF$, this relation yields a ratio $\varphi_1/\varphi_2 \approx 0.6$.

[9] In order to measure an electric field larger than 100 V m^{-1}, the SDA design was modified by inserting a

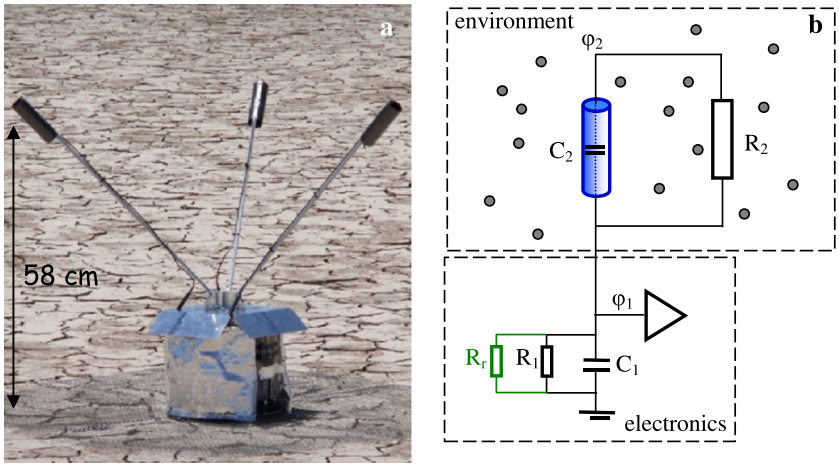

Figure 2. (a) SDA instrument. (b) A simplified schematic of electronics-electrode-environment electrical configuration.

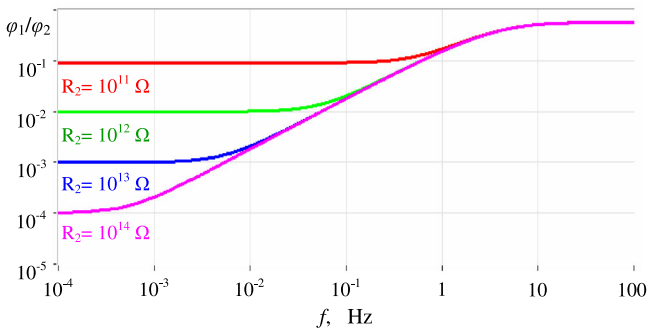

Figure 3. φ_1/φ_2 versus frequency for various values of the R_2 resistance. R_r is fixed at 10GΩ.

resistance R_r at the electronics input (Figure 2b). This resistance has a value much lower than that of the input resistance R_1. In this configuration, the ratio φ_1/φ_2 can be written as

$$\varphi_1/\varphi_2 = (1 + i\omega C_2 R_2)/((R_r + R_2)/R_r + i\omega(C_1 + C_2)R_2). \quad (2)$$

[10] Thus, if the value of the resistance R_r is also much lower than that of the coupling resistance R_2, the measured electric potential φ_1 is reduced by a factor R_r/R_2 with respect to the potential φ_2 found at the electrode level in the unperturbed environment. For example with $R_r = 10^{10}$ Ω and $R_2 = 10^{13}$ Ω, the measured electric potential of 10 V corresponds to 10 kV at the electrode level. The variations of φ_1/φ_2 versus the linear frequency ($f = (2\pi)^{-1}\omega$) are presented in Figure 3 for four values of the coupling resistance R_2 between 10^{11} and 10^{14} Ω and $R_r = 10^{10}$ Ω. In general, the value of the R_r resistance is chosen by considering the electrical properties of the environment where the measurements are performed, specifically its electric resistivity and the expected amplitudes of the electric field.

[11] In the case when $R_2 \gg R_r$, the electrode potential is significantly smaller than the potential found at the electrode height in unperturbed air. This difference produces a perturbation of equipotential lines in the vicinity of the electrode. These perturbations must be estimated and factored into the calculations for the electric potential of the unperturbed environment. In order to get a quantitative estimate of the perturbations induced by the electrode, the charge distribution on the electrode surface is calculated using the numerical method developed by *Kolesnikova* [1997]. The surface charge is determined from the external electric field and the electrode's electric potential. The distribution of the electric potentials near the electrode is then calculated as the sum of two contributions, (i) the external electric field and (ii) the surface charges. The left panel of Figure 4 represents the equipotential contours around the electrode at 0 V in a uniform electric field. Electric potentials are normalized to the value of the electrode potential in the configuration when the electrode is floating. The equipotential line enclosing the electrode corresponds to the normalized value of $k_\varphi = 0.62$, while the equipotential line with normalized value of 1 is displaced upward.

[12] The computations presented above do not include the mast that supports the electrode nor the cable used to transmit the signal from the electrode to the electronics box. The effects of the mast and the cable are discussed and evaluated below.

[13] The SDA mast is a fiberglass tube with an external diameter of 8 mm and internal diameter of 6 mm. The relative permittivity of the fiberglass composite is ~5. The electric perturbations induced by this mast are estimated to be small and are undetectable at a distance of 1.5 cm (approximate radius of electrode) from the mast axis.

[14] The cable running along the mast is a coaxial cable with a tinned copper shield of 0.98 mm external radius. This shield, being bootstrapped (i.e., connected to the output of the input preamplifier with a gain of 1), slightly modifies the distribution of potential contours around the electrode. The right panel of Figure 4 represents the equipotential contours around the electrode when a coaxial cable of 40 cm length is included in the model. Similar to the results shown on the left panel (model without cable), the induced perturbations reduce the value of electric potential at the electrode height with respect to its value in unperturbed air. The reduction coefficient is estimated to be $k_\varphi = 0.54$ (with respect to 0.62 found in the model without the cable). The perturbations of the equipotential lines also cause an increase in the electric field near the electrode surface. The electric field near the electrode surface is calculated to be k_E = 17 times higher than its value in unperturbed air. Both coefficients, k_φ and k_E, are then used in estimating the electric features of atmosphere at the electrode height.

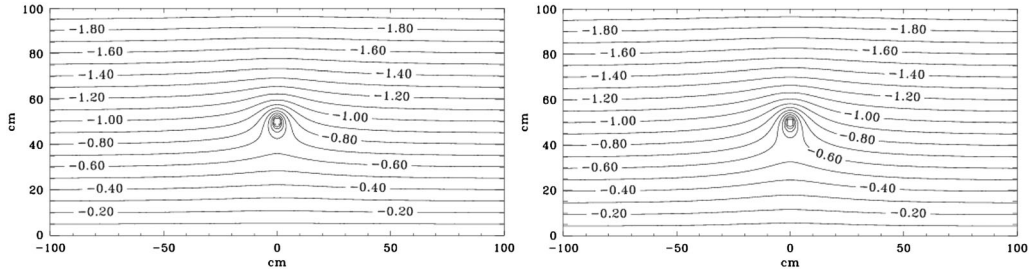

Figure 4. Equipotential contours around the SDA electrode at 0 V in (left) the model without cable and in (right) the model with coaxial bootstrapped cable.

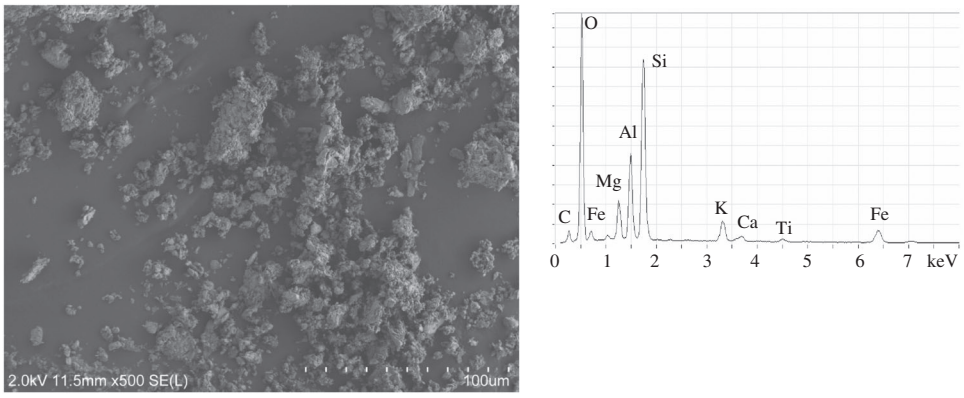

Figure 5. (left) Image of a soil sample from the playa, made with a scanning electron microscope (SEM). Energy of the SEM electron beam was fixed at 2 keV. The scale shown is in 10 μm increments. (right) A typical energy-dispersive X-ray spectrum of the soil sample. Energy of the SEM electron beam was fixed at 15 keV.

[15] The coupling resistance R_2 introduced in the simplified schematic of Figure 2b is a quantity that depends not only on the electric resistivity of the atmosphere but also on the measurement method and the instrument geometry. Thus, the relationship between the coupling resistance and the resistivity of the air needs to be discussed and evaluated. According to Ohm's law, the resistance is used in relationship between the electric current and the electric potential difference ($I = \Delta\varphi/R$), while the resistivity is used in relationship between the electric current density and the electric field ($j = E/\rho$). Thus, the first term is given in Ω, while the second in Ω m. The current that circulates in the vicinity of the SDA electrode is different from that in the unperturbed air because of an increase in the electric field induced by the electrode. The relationship between this current, I, and the current density in unperturbed air, j_0, can be written as

$$I = j_0 s k_E, \tag{3}$$

where s is the current collection area of the SDA electrode and k_E is the ratio of the electric field near the electrode surface with respect to the unperturbed electric field. The relationship between the coupling resistance R_2 and the air resistivity ρ is then deduced from (3), by $I = \frac{\varphi_2 - \varphi_1}{R_2} \approx \frac{k_\varphi \Delta\varphi}{R_2} = \frac{\Delta\varphi}{\Delta z \rho} s k_E$, where Δz is the height of the SDA electrode with respect to the ground. Thus,

$$\rho = R_2 \frac{s}{\Delta z} \frac{k_E}{k_\varphi}. \tag{4}$$

[16] Substituting the parameters corresponding to the SDA configuration, $s = 0.94 \cdot 10^{-2}\text{m}^2$, $\Delta z = 0.58$m, $k_\varphi = 0.54$, and $k_E = 17$, we find $\rho \approx 0.5 R_2$. This relationship will be used below in section 5.2.

2.3. Wind Sensors

[17] The wind was measured with two ultrasonic anemometers. A two-axis anemometer was installed 6 m from the SDA instrument, between the SDA and FM sensors (Figures 1a and 1b), to measure the horizontal wind at 50 cm above the ground. A three-axis anemometer was mounted on the top of the FM mast, 2 m from the ground. As measured by the anemometers, a wind from the south corresponded to 180° and a wind from the east to 90°. The temporal resolution was 0.25 and 0.1 s, respectively, for the two-axis and three-axis anemometers.

3. Field Site and Environmental Conditions

3.1. Field Site

[18] Our field campaign was carried out in July 2011 on the Eldorado Dry Lake southwest of Boulder City in the U.S. State of Nevada. A "Dust Hazard" sign along the highway that crosses the Eldorado Valley indicates the frequent dust activity in the area. The northern end of the valley contains a natural dry basin, the surface of which is hard, barren, and flat with mud cracks that break up the surface. Strong winds, which are ubiquitous on the lake and the surrounding area (flat fields covered with sparse low vegetation), regularly generate blowing dust. Over 840 dust devils were observed and characterized during previous summer field campaigns in 1995 and 1996 [*Metzger*, 1999]. The dust activity typically extends from around 10 to 18 local time (LT) and is highest in the early afternoon when the ground temperature approaches 60°C and the near-ground air is heated above 30°C. The morphology of the dust devils is observed to vary from a sharply defined column of rotating dust to a disordered dust cloud with little structure.

3.2. Soil Properties

[19] The soil of the Eldorado field site is composed of abundant and diverse clays, evaporate- and carbonate-bonded aggregates, various sizes of quartz fragments, organic binder, and fine sediments [*Metzger*, 1999]. Most of the individual dust particles have a size less than few micrometers but can form clumps and larger fragments as the particles adhere to each other. An image of a soil sample from the playa, made with a scanning electron microscope, is shown on the left panel of Figure 5 to give a sense of the dust morphology and size distribution.

[20] Electric properties of the soil and thus of the airborne grains are determined by the soil composition. A typical energy-dispersive X-ray spectrum obtained by excitation of the soil sample with a 15 keV electron beam is presented in

Table 1. Atomic Composition of the Soil Samples Deduced From the X-ray Spectra

Element	O	Na	Mg	Al	Si	K	Ca	Ti	Fe
Mean atomic %	64	0.6	3.3	6.8	16.1	3.3	0.5	0.5	4.9
Standard deviation %	4.9	0.1	0.8	0.5	2.6	0.8	0.2	0.2	1.5

the right panel of Figure 5. Each emission line corresponds to the migration of the electron from the outer (L) to the inner (K) electron shell (with exception of the emission at ~0.7 keV which is likely generated by the migration from M to L shell of the iron atom). The X-ray spectra of four soil samples were analyzed with the aim of deducing the average atomic composition. The mean values and the estimated standard deviation of the atomic composition are presented in Table 1. Note that each soil sample was spattered by a thin carbon layer in order to avoid the electric charging of the sample and its support. For this reason, the carbon line observed in the X-ray spectra was not included in Table 1. All elements found in the soil samples are common among the most abundant minerals of the Earth's surface such as, quartz, calcite, feldspar, and mica. The relative permittivity of each of these minerals in pure state is estimated to be approximately 4 for quartz, 8 for calcite, 5 for feldspars, and 4–9 for mica. The difference in the relative permittivity of the individual grains is likely an essential parameter that determines the charge and the charge polarity of each grain due to grain-grain contact.

3.3. Instrument Placement

[21] The placement of instruments at the field site is illustrated in Figure 1. The FM and SDA sensors were placed 20 m apart in order to be sufficiently close to each other to observe the same events, but sufficiently far to avoid mutual electric perturbations. Being very unstable and variable, the wind had a prevailing direction along the valley and came from the south. Orientation and relative position of the instruments on the field site were driven by this wind. The four FM sensors were pointed toward the west in order to measure the electric field in a vertical plane oriented north-south. All instruments were aligned in the north-south direction.

3.4. Environmental Conditions

[22] The meteorological conditions were typical for Eldorado Valley in July, i.e., clear sky, hot, and dry, with variable wind. The observations presented in our paper were made in the early afternoon, around 13 LT, when the near-ground air continued to increase in temperature (~1°C per 20 min) and reached +42°C during the observations. The average air pressure was 946 hPa.

[23] The prevailing wind (see Figure 10d) came from the south (180° as measured by anemometer), south-east (135°). The total horizontal wind speed varied between 2 and 9 m s^{-1} at 50 cm above the ground and increased with height up to ~13 m s^{-1} at 2 m. The vertical wind speed fluctuated around zero with the maximum not exceeding ~1 m s^{-1}. Wind structures with sheared vertical wind, like that presented in Figure 2 of *Metzger et al*. [2011], were periodically seen in the 2 s averaged data. The ascendant air motion was recurrently observed at the moments when the horizontal wind slowed. The shear structures were persistent in the wind data and were likely caused by air instabilities. Not all of them were associated with an increase of the electric field (see section 6).

[24] The Eldorado site is surrounded by numerous high power transmission lines in addition to a solar power station located to the south of the playa. To evaluate the potential impact of the power lines on the electric field measurements, preliminary tests of the SDA instrument were conducted on the site in May 2011 (2 months before the campaign). These tests led to the conclusion that (a) the emitted power (which is measured to be less than approximately 10 mV^2/Hz) does not saturate the SDA dynamics, (b) the emission lines are narrow and stable, and (c) simple filtering of 60 Hz and its harmonics is sufficient to remove the power line signal from the SDA data. The rotational (and thus working) frequency of the FM instrument is 20 Hz. Consequently, the electric field deduced from the FM measurements was not perturbed by the power line emissions.

4. Vertical Profile of the Electric Field

4.1. FM Measurements

[25] We start the data analysis with one example of the FM measurements at various heights presented in Figure 6. The first 60 s of data correspond to the measurements in the absence of visible dust lifting, with the electric field pointed downward. Hereafter, such periods are called "quiet." During the last 40 s of the measurements, we observed dust blowing across the instruments site and the FM sensors measured an increased upward electric field. Hereafter, such periods are called "active." The electric field is nearly uniform at the heights from ~0.5 to 2 m, but varies significantly in the vicinity of the ground. An essential increase of the electric field in the near-ground layer of ~20 cm was previously observed with FM instrument and reported by *Schmidt et al*. [1998].

[26] There are at least two mechanisms that can produce a height variation of the electric field, electric charging of the soil surface, and/or noncompensated space charges.

[27] The FM sensing cylinder is plated with gold, thus, we do not expect a charge to accumulate on the sensor surface other than that induced by the electric field perpendicular to its surface. In a uniform electric field, the total electric charge on the sensing cylinder is zero. In a nonuniform electric field, electric charges induced on the opposite sides of the sensor are not compensated locally, but by the surface charge

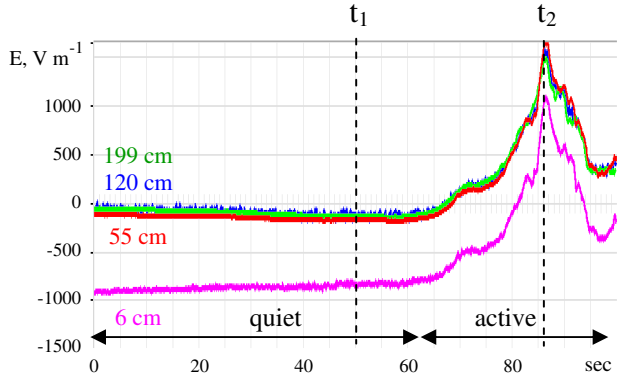

Figure 6. Vertical component of electric field measured by FM sensors at four heights. Positive/negative values correspond to upward/downward electric field.

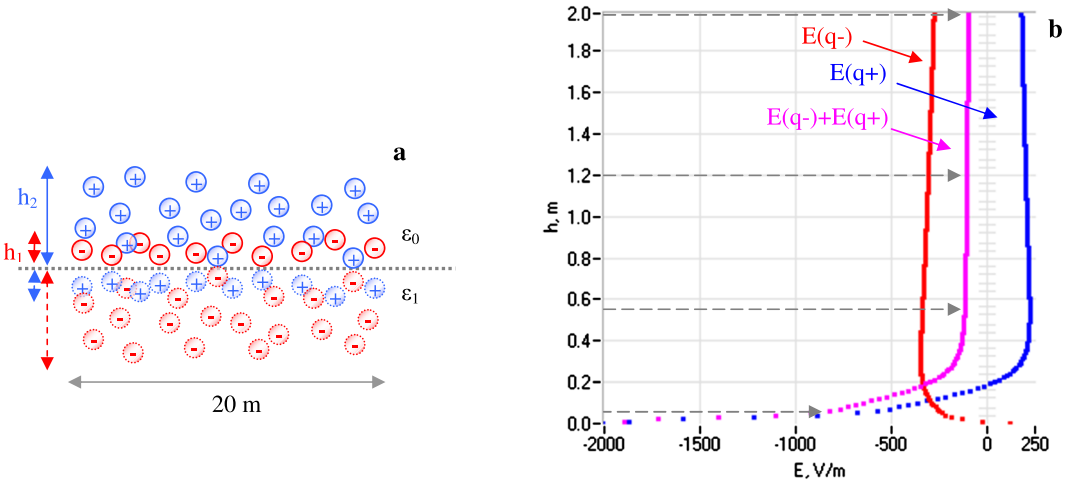

Figure 7. (a) Quiet case model for two layers of uniformly distributed test particles with opposite charges and their image charges. (b) Vertical electric field computed in the center of the layers: $E(q+)$ and $E(q-)$ correspond to the electric field produced by the layers of positive and negative charges, $E(q+)+E(q-)$ is the total electric field. The heights of the layers with negative and positive electric charge are $h_1 = 0.5$ cm and $h_2 = 15$ cm, respectively. The electric charge concentration in each layer is $5.2 \cdot 10^{13}$ and 10^{12} electrons m^{-3}, respectively.

induced on the ground. However, the induced surface charges do not significantly modify the initial electric field. The perturbations at the heights above 6 cm from the ground are estimated to not exceed 3% of the initial electric field.

[28] In the following section, we examine the contribution of the space charge in the electric field measurements.

4.2. Contribution of Space Charge in the Electric Field Measurements

[29] Due to triboelectric charging, the soil grains and the airborne particles might gain a number of elementary charges. The polarity of the charge carried by each particle depends on its dielectric properties and also on the dielectric properties of both the surface and levitating material. Since an excess of one polarity of charge creates an electric field, the height profile of the electric field is determined by the height distribution of the charge and its polarity. In this section, we present a simple model that allows the simulation of the charge distribution. This charge distribution is then used to compute the resulting electric field. The proposed model comprises two layers of uniformly distributed particles with opposite sign and their image charges. Each randomly generated test particle represents a number of particles that carry a number of elementary charges. The parameters, such as effective diameter and height of the dust/sand layer, sign of the charge carried by a test particle and "weight" of each test particle (i.e., number of particles times number of elementary charges) are varied with aim to recreate the observed profile of the electric field. Two conditions are considered and simulated here: the first corresponds to the quiet and the second to the active periods represented in Figure 6.

[30] The quiet case model comprises two layers (Figure 7a). The first layer consists of negatively charged particles with a charge density of $5.2 \cdot 10^{13}$ electrons m^{-3} and height of 0.5 cm. The second layer consists of positively charged particles with a charge density of 10^{12} electrons m^{-3} and height of 15 cm. Profiles of the vertical electric field produced by the charges found in each layer and the corresponding image charges are shown in Figure 7b. The fields are calculated at the center of 20 m diameter cylindrical layer. The total electric field shown in the same figure is negative (i.e., downward pointing) and nearly constant above 40 cm, but varies considerably near the surface. At the heights of two FM sensors, 6 and 55 cm, the electric field is calculated to be 820 and 115 V m^{-1}, respectively. The modeled values are very similar to the FM sensors measurements at time t_1 in Figure 6.

[31] Similar to the quiet case, the conditions of dust activation (active case) are modeled by two layers of suspended particles. Unlike in the quiet case, the layers extended up to a few meters above the surface (Figure 8a). The positive charges are uniformly distributed in a 2.2 m layer, while the negative charges fill a layer that is 4 m tall. The charge density in both layers is approximately 10^{11} electrons m^{-3}. The electric fields induced by the charges of each layer and the corresponding image charges are shown in Figure 8b. The variation of the total electric field with the height is presented in the same figure. The computed electric field is nearly constant up to a height of ~2 m, positive (i.e., upward pointing) up to a height of ~3.3 m and very similar to the electric field measured by the FM sensors above 50 cm (Figure 6). In order to get the electric field observed by the FM below 50 cm, the computed electric field (Figure 8b) is superposed with that found in the quiet case model (Figure 7b). The resulting electric field has an amplitude ~1700 V m^{-1} at the heights comprised between 40 cm and 2 m. Below 40 cm, its amplitude exponentially decreases with height and attains ~1000 V m^{-1} at 6 cm. The computed values are found to be very close to those measured by the FM sensors at time t_2 indicated in Figure 6.

5. Electric Resistivity of Air

5.1. From Electric Field to Electric Potential

[32] In order to calculate the electric potential, φ, from the electric field, E, measured by two FMs at two heights, z and

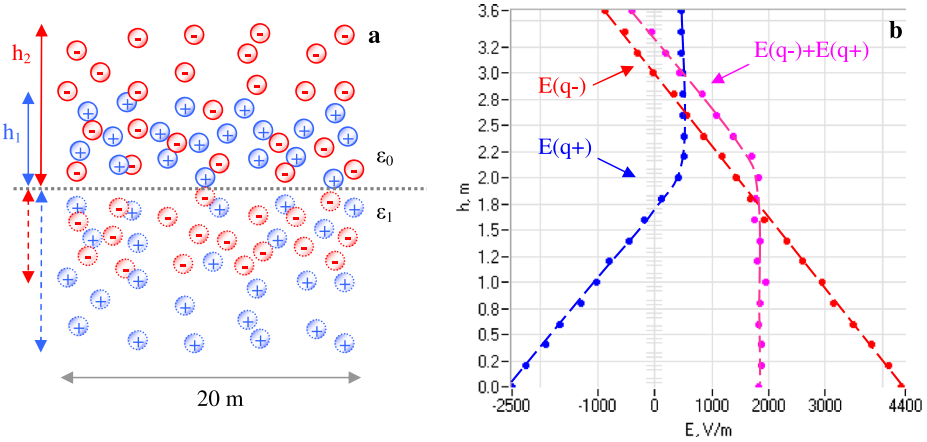

Figure 8. (a) Active case model for two layers of uniformly distributed test particles with opposite charges and their image charges. (b) Vertical electric field computed in the center of the layers: $E(q+)$ and $E(q-)$ correspond to the electric field produced by the layers of positive, negative charges, $E(q+)+E(q-)$ is the total electric field. The heights of the layers with positive and negative electric charge are $h_1 = 2.2$ m and $h_2 = 4$ m, respectively. The electric charge concentration in each layer is ~10^{11} electrons m^{-3}.

z_0, the equation $E_z = -\frac{d\varphi}{dz}$ is integrated over the interval [z_0, z]. Using the trapezoid rule for approximating the definitive integral, this can be written as

$$\int_{z_0}^{z} E_z dz \approx 0.5(E_z(z) + E_z(z_0))(z - z_0) = -(\varphi(z) - \varphi(z_0)). \quad (5)$$

[33] Solution (5) is an exact solution of the integral if the electric field is constant or varies linearly with height, but it becomes an approximation if the variation is nonlinear.

[34] With the aim of comparing two sets of observations, we use the potential, $\Delta\varphi_{SDA}$, measured by the SDA electrode at 58 cm with respect to the ground, and the potential deduced from the electric field measured by the FM sensors at 55 and 6 cm. The electric field profiles computed in the two-layer model (section 4.2) are used to test the method and estimate its accuracy. The difference of the potentials calculated via (5) from the modeled electric field at 55 and 6 cm is found to be 229 V, while the difference of the potentials between the height of 58 cm (the height of the SDA electrode) and the ground is estimated to be 225 V. Thus, two sets of observations give approximately the same values.

5.2. Coupling Resistance and Electric Resistivity of Atmosphere

[35] Following the discussions presented in section 2.2, the potential measured by the SDA in the configuration with a voltage divider is determined by two parameters, (i) the potential at the electrode height and (ii) the coupling resistance between the electrode and the atmosphere. The coupling resistance is a quantity that depends not only on the electric resistivity of the atmosphere but also on the measurement method and the instrument geometry. The relationships between the potential at the electrode height, the measured potential, the coupling resistance, and the air resistivity are evaluated in section 2.2 and used in this section. In order to illustrate the proposed method, we consider 30 min of observations that comprise a few periods of dust activation (and associated negative electric potential minima on the order of kV) followed by quiet periods (and corresponding positive electric potential). The data recorded by the two instruments are reported in Figures 9a and 9b; Figure 9a shows the potential measured by the SDA electrode at the height of 58 cm and Figure 9b demonstrates the potential deduced via equation (5), shown in green, from the FM electric field measurements at 6 and 55 cm. For a fixed value of the coupling resistance R_2, the electric potential difference between the height of the SDA electrode and the ground can be computed using the potential measured by the SDA (Figure 9a). For this we make a Fourier transformation of the measured signal (φ_1), apply equation (2) to find the spectral power of the electric potential φ_2 at the electrode level, and then make the inverse Fourier transformation. In order to get the potential at the electrode height in unperturbed air, the deduced potential is then divided by the k_φ reduction coefficient, introduced in section 2.2. The resulting potential is presented in Figure 9b, shown in blue, and corresponds to the value of the coupling resistance $R_2 = 4 \cdot 10^{13}$ Ω. The two lines, green and blue, follow each other in shape and fit each other in amplitude for most of the period. The value of the coupling resistance is then varied in order to get the best fit of the potentials during the whole 30 min period. The black line in Figure 9b shows the variation of the coupling resistance that provides the best fit of two data sets. The coupling resistance varies between $3 \cdot 10^{13}$ and $1.2 \cdot 10^{14}$ Ω. According to equation (4) in section 2.2, the resistivity of atmosphere is proportional to the coupling resistance and for the SDA configuration is estimated to vary between $1.5 \cdot 10^{13}$ and $6 \cdot 10^{13}$ Ω m. The variations of the coupling resistance and thus the resistivity of air are likely associated with variations in the concentration of the light ions, which are the main carriers of electrical currents in the lower atmosphere. An increase in resistivity just after the event centered around 7 min indicates a formation of a "high resistive tail" behind the dust cloud that passed through the instrumental site and had a horizontal speed significantly higher than that of the ambient air. Seven minutes are then required to recover the resistivity level preceding the event. With respect to other events, the event observed around 7 min is not followed by wind rotation; see grey line in Figure 9d. Little exchange with

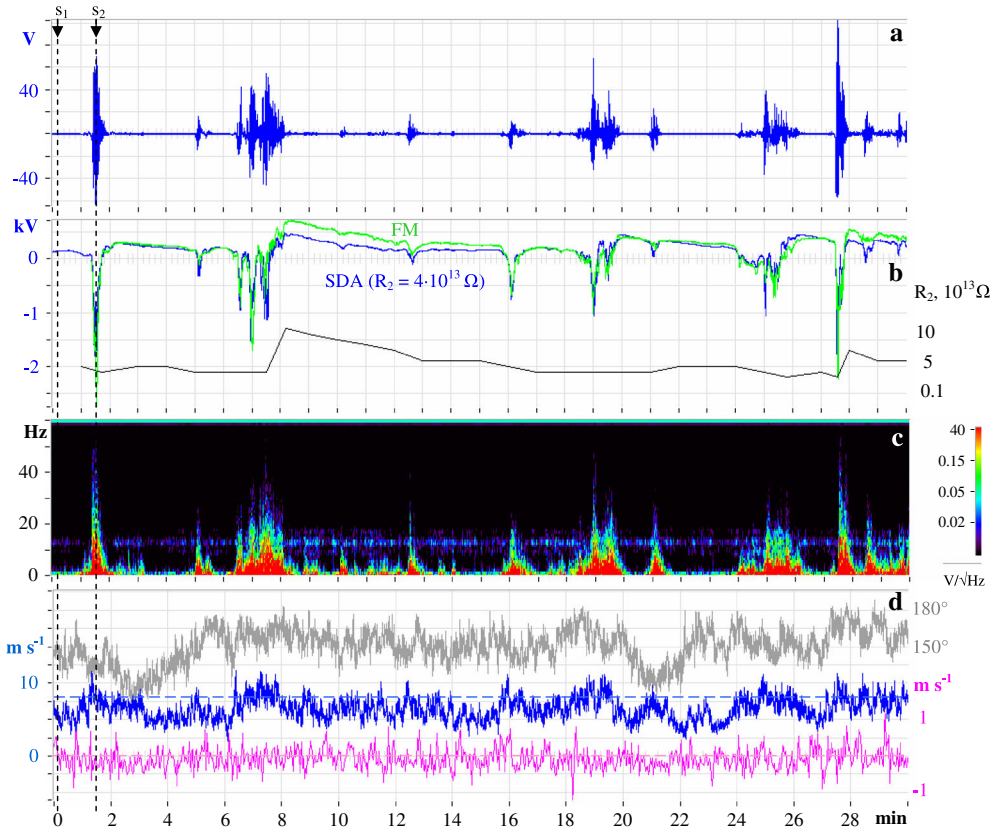

Figure 9. (a) Electric potential measured by the SDA electrode. (b) Electric potential deduced from the electric field observed by the FM sensors at 6 and 55 cm (green line) and from the SDA measurements under the assumption that $R_2 = 4 \cdot 10^{13}$ Ω (blue line). The coupling resistance deduced from the best fit of the FM and SDA, is shown by the black line. (c) Spectrogram of low frequency emissions measured by the SDA electrode. (d) Wind direction (grey), total horizontal wind velocity (blue), and 2 s averaged vertical wind velocity (magenta). Upward/downward wind corresponds to the positive/negative values.

the ambient (unperturbed) air in the nonrotational flow likely determines the electric properties of the air downstream the dust cloud.

6. Low-Frequency Electrostatic Emissions

[36] Dust motion and its electrical charging not only produce variations in the DC electric field but also generate an increase in the low-frequency AC component of the electric field. In order to illustrate this, the temporal evolution of the power spectra in the signal measured by the SDA is computed for the 30 min period presented in Figure 9. For this, the whole period is divided into equal subperiods. Hann windowing is applied inside each subperiod in order to reduce the Fourier transformation edge effects. Spectral power is then calculated at 60 discrete frequencies of 1 Hz width and is presented in a color scale. Two emissions at 60 Hz and 13 Hz are clearly seen in the spectrogram shown in Figure 9c. The 60 Hz signal is the first harmonic of the nearby power transmission lines (see section 3.4), while the peak at 13 Hz corresponds to the mechanical resonance of the SDA mast. A comparison of the data presented in Figure 9 indicates that (i) each increase of DC electric potential is associated with low-frequency emissions and (ii) each burst of the low-frequency emissions is related to an increase in the total horizontal wind speed above 7 m s^{-1}; see horizontal blue line in Figure 9d.

[37] Ultralow frequency emissions associated with dust devils were previously observed with a magnetic search coil instrument [*Houser et al.*, 2003, *Farrell et al.*, 2004] and were suggested to be generated by the cyclonic motion of electrically charged dust. The observations presented in our paper comprise the sequence of quiet periods followed by the phases of dust activation with disordered dust clouds blowing through the observation site rather than sharp dust columns with well-formed rotation. Moreover, even during quiet periods (no visible dust blowing through the instrumental site), an increase of the low-frequency power is observed by the SDA electrode. In order to illustrate this, two measured frequency spectra are presented in Figure 10. The first spectrum, shown as a black line in Figure 10a, corresponds to the SDA signal measured around time "s1" (indicated by a vertical arrow in Figure 9), while the second spectrum, shown as a black line in Figure 10b, corresponds to the SDA data around time "s2." Thus, the first sequence (s1) is recorded during quiet conditions (weak wind, downward electric field of ~200 V m^{-1}), while the second (s2) is measured during active conditions (increased wind speed, upward electric field of few kV m^{-1}). Both spectra show an increase in low-frequency power, below ~50 Hz for s1 and below ~150 Hz for s2, but differ by ~10^3 in amplitude.

[38] Under the conditions when the electrical features of the air are controlled by the motion and the electric charging of the

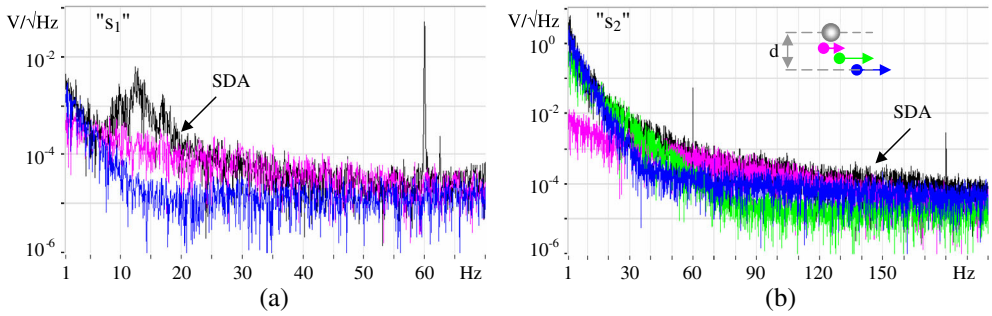

Figure 10. Frequency response deduced from the temporal variation of the electrode potential measured by SDA electrode (black line) during a 20 s period centered at the moments (a) s_1 and (b) s_2 indicated in Figure 9 and calculated from the test particle model (colored lines). Each color represents the frequency spectrum induced by a straight-line motion of test particles at 1 cm (magenta), 10 cm (green), and 20 cm (blue) from the electrode. Particles speed is fixed at (a) 4 m s^{-1} and (b) 6 m s^{-1}.

dust/sand particles, the electric potential measured by an electrode is mainly determined by the charge carried by each grain, the concentration of charged particles, and the distance that separates the particle from the electrode. In consequence, a change of one or few of these parameters can produce a temporal variation of the electric potential. Variation of the electric charge on each grain depends on the characteristic frequency of its contact with other particles (e.g., collision frequency for levitating particles, ballistic period for saltating sand grains, etc.) and on the number of elementary charges gained or lost due to each contact. Variation of the distance between a charged particle and the electrode is defined by the particle speed and its trajectory with respect to the electrode. In an attempt to quantify the effect of the dust/sand motion on the frequency spectra of the measured electric potential, a simple model is proposed and discussed below. The ensemble of dust/sand grains is represented by test particles moving with a constant speed along a straight line. Each trajectory is characterized by a distance d (see drawing in Figure 10b), which is the closest distance between the particle and the electrode represented as a sphere. The electric charge carried by each test particle is a parameter, which is varied in order to get the spectral power close to that measured by SDA (black line in Figure 10). The temporal variation of the electrode potential induced by the motion of the test particles, superposed with a white noise of 10 μV/√Hz (sensibility of SDA electronics calculated for 20 s data), is then transformed (Fourier transformation with Hann windowing) into the frequency domain. The computed frequency response is shown in Figure 10. Different colors stand for the spectra produced by the straight-line motion of the test particles at $d = 1$ cm (magenta), $d = 10$ cm (green), and $d = 20$ cm (blue) with respect to the electrode. It is assumed that all particles move with the same velocity, 4 m s^{-1} for the spectra presented in Figure 10a and 6 m s^{-1} in Figure 10b. These velocities are chosen to match the average horizontal wind velocity at the moments s1 and s2. Black lines in Figures 10a and 10b represent the spectra deduced from the 20 s SDA signal recorded at the moments s1 and s2. Comparison of the modeled and the measured spectra demonstrates a clear relationship between the distance at which the particle passes with respect to the electrode and the shape of the frequency spectra. Those particles that pass closer to the electrode cause more rapid temporal variations of the electrode potential and thus, produce spectral perturbations in a larger frequency band. For example, presented in Figure 10a, an increase of the measured power (black line) in the frequency range from ~20 to 50 Hz matches with the spectrum corresponding to the motion of the test particles at $d = 1$ cm with respect to the electrode (magenta line), while the spectral shape measured below ~5 Hz corresponds to the spectral variation found in the model with the particle trajectories at 20 cm with respect to the electrode. A similar effect is reproduced for the spectra shown in Figure 10b. These spectra correspond to the conditions with increased dust speed (6 m s^{-1}) and higher charge concentration (~50 times more that that found for the spectra presented in Figure 10a). The resulting (measured and simulated) increase of the spectral power is observed up to a frequency of ~150 Hz. This increase and also the form of the power spectra are mainly determined by the charge concentration.

[39] The proposed model demonstrates that the motion of electrically charged dust/sand in the vicinity of the electrode creates an increase of the spectral power at the frequencies below 200 Hz, in the ULF/ELF frequency range. Spectral features of these emissions are determined by a number of parameters, such as the charge concentration, its variation at different heights, and the particle speed with respect to the electrode. Of course, other parameters like collision frequency and number of the elementary charges that are lost or gained during each contact might also control the shape of the frequency spectra. In future studies, more sophisticated modeling might also consider the complex reality of particle transport (i.e., particle transport lag to the wind speed, nonparallel and nonstraight-line particle trajectories) and take into consideration the exact shape of the electric field sensor.

7. Conclusions

[40] We have presented the measurements performed in Eldorado Valley with a suite of electric field instruments and showed the advantages of this instrument combination.

[41] Simultaneous measurements with the FM and SDA allow the deduction of the coupling resistance between the SDA electrode and the atmosphere. This resistance can then be used to estimate the electric resistivity of the air. The electric resistivity of the air is found to vary between $1.5 \cdot 10^{13}$ and $6 \cdot 10^{13}$ Ω m during a 30 min period when several dust clouds were observed to pass through the instrumentation

site. Each pass of a dust cloud is associated with an increase in the upward electric field of up to 6 kV m^{-1} and a reduction in the electric resistivity.

[42] The high sensibility and large frequency range of the SDA instrument allow it to measure AC electric fields concurrently with DC. An increase of spectral power at frequencies below ~50 Hz is observed even during relatively quiet periods (without visible dust blowing). Each increase of the DC and the low-frequency AC electric field corresponds to an increase in the wind speed above ~7 m s^{-1}. We demonstrated that the measured spectra could be simulated by a simple model where electrically charged particles move in a straight-line motion near the electrode. Three parameters control the frequency response in this case, (i) the minimum distance between the particle and the electrode, (ii) the charge concentration, and (iii) the particle speed.

[43] The electric field measured by the FM instrument mounted at 6 cm from the ground often differed from that observed above 50 cm. A simple multilayer model was proposed to reproduce the height profile of the electric field. According to this model, even under quiet conditions (downward electric field of a few hundred of V m^{-1}), the near-surface layer (tens of centimeters thick) is filled with electrically charged dust/sand particles with a predominantly negative charge in the vicinity of the soil. The charge concentration inside the layer was estimated to vary between 10^{12} and $5 \cdot 10^{13}$ electrons m^{-3}.

[44] A more comprehensive testing of the methods and models developed in this paper is left for future field campaigns. For example, in order to ensure the precision of the estimated electric resistance, two SDA electrodes will be mounted at two different heights from the ground and above 50 cm. Concurrent measurement of the electric field and the airborne dust/sand will be the major objective of our future studies. These observations will improve our model relating the electric field with the height distribution of the electric charge and permit a greater understanding of the mechanisms for the dust/sand electric charging.

Appendix A: Electric Perturbations Induced by SDA Reference Box

[45] In order to get quantitative estimates of the perturbations induced by the electrically grounded body, the charge distribution on the box surface and on the ground is calculated [*Kolesnikova*, 1997]. The surface charges are determined by the initial electric field and the ground electric potential. The distribution of the electric potentials in the vicinity of the reference body is then calculated as a sum of two contributions, the initial electric field, and the surface charges. An example, shown in Figure A1, corresponds to the upward electric field, variation of which with the height, z, follows an exponential law $E(z) = -1000 \cdot e^{-z/0.1} + 2000$. Such variation corresponds approximately to the electric field observed by the FM sensors during a period of dust activation (Figure 6). The perturbations of the electric potential at the height of the SDA electrode induced by the surface charges are estimated to not exceed 1%. As one would expect, the induced perturbations increase with a decrease in the distance between the electrode and the reference surface. Thus, for a mast of 9 cm in length (half of the box height), the measured potential will be underestimated at about 17 %.

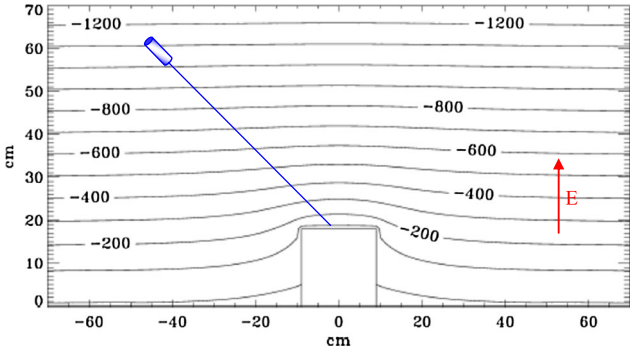

Figure A1. Distribution of equipotentials in the vicinity of the SDA reference box in conditions of upward exponentially varied electric field. The ground potential is set to 0 V.

[46] **Acknowledgments.** The SDA instrumental development and organization of the Nevada campaign were financially supported by CNES and IPSL. Special thanks to F. Vivat (LATMOS) and S. Musko (SPRL) who, respectively, developed the software for SDA and FM data acquisition. We thank P.-Y. Meslin (IRAP) and high school students M. Szocik and S. Kim for their help in the field campaign. We thank also D. Brouri for help with SEM imaging.

[47] Masaki Fujimoto thanks Stephen Metzger for assistance in evaluating this paper.

References

Balme, M., and R. Greeley (2006), Dust devils on Earth and Mars, *Rev. Geophys.*, *44*, RG3003, doi:10.1029/2005RG000188.

Farrell, W. M., G. T. Delory, S. A. Cummer, and J. R. Marshall (2003), A simple electrodynamic model of a dust devil, *Geophys. Res. Lett.*, *30*(20), 2050, doi:10.1029/2003GL017606.

Farrell, W. M., et al. (2004), Electric and magnetic signatures of dust devils from the 2000–2001 MATADOR desert tests, *J. Geophys. Res.*, *109*, E03004, doi:10.1029/2003JE002088.

Greeley, R., and J. D. Iversen (1985), *Wind as a Geological Process on Earth, Mars, Venus, and Titan.*, pp. 333, Cambridge Univ. Press, New York.

Houser, J. G., W. M. Farrell, and S. M. Metzger (2003), ULF and ELF magnetic activity from a terrestrial dust devil, *Geophys. Res. Lett.*, *30*(1), 1027, doi:10.1029/2001GL014144.

Johnston, A. R., and H. Kirkham (1989), A miniaturized space-potential DC electric field meter, *IEEE Trans. Power Delivery*, *4*(2), 1253–1261.

Kok, J. F., and N. O. Renno (2006), The effects of electric fields on dust lifting, *Geophys. Res. Lett.*, *33*, L19S10, doi:10.1029/2006GL026284.

Kok, J. F., and N. O. Renno (2008), Electrostatics in wind-blown sand, *Phys. Rev. Lett.*, *100*, 014,501.

Kolesnikova, E. (1997), Méthode des distributions superficielles de charges pour la modélisation des antennes électriques en plasma homogène, isotrope et Maxwellien, *Thèse de Doctorat*, Univ. Orléans.

Merceret, F. J., J. G. Ward, D. M. Mach, M. G. Bateman, and J. E. Dye (2008), On the magnitude of the electric field near thunderstorm-associated clouds, *JAMC*, *47*, 240–248.

Metzger, S. (1999), Dust devils as Aeolian transport mechanisms in southern Nevada and Mars Pathfinder Landing Site, PhD dissertation, University of Nevada, Reno.

Metzger, S. M., M. R. Balme, M. C. Towner, B. J. Bos, T. J. Ringrose, and M. R. Patel (2011), In situ measurements of particle load and transport in dust devils, *Icarus*, *214*, 766–772, doi:10.1016/j.icarus.2011.03.013.

Renno, N. O., J. F. Kok, H. Kirkham, and S. Rogacki (2008), A miniature sensor for electric field measurements in dusty planetary atmospheres, *J. Phys., Conf. Ser.*, *142*, 012075, doi:10.1088/1742-6596/142/1/012075.

Schmidt, D. S., R. A. Schmidt, and J. D. Dent (1998), Electrostatic force on saltating sand, *J. Geophys. Res.*, *103*(D8), 8997–9001.

Sickafoose, A. A., J. E. Colwell, M. Horányi, and S. Robertson (2001), Experimental investigations on photoelectric and triboelectric charging of dust, *J. Geophys. Res.*, *106*(A5), 8343–8356.

Stolzenburg, M., and T. C. Marshall (1998), Charge precipitation and electric field in two thunderstorms, *J. Geophys. Res.*, *103*(D16), 19,777–19,790.